Emergence of band structure in a two-dimensional metal-organic framework upon hierarchical self-assembly

Daniel Baranowski[a,], Marco Thaler[b], Dominik Brandstetter[c], Andreas Windischbacher[c], Iulia Cojocariu[a,d,e], Simone Mearini[a], Valeria Chesnyak[e,f], Luca Schio[f], Luca Floreano[f], Carolina Gutiérrez Bolaños[d,†], Peter Puschnig[c,*], Laerte L. Patera[b,*], Vitaliy Feyer[a,g,*] and Claus M. Schneider[a,g,h]*

[a]Peter Grünberg Institute (PGI-6), Jülich Research Centre, 52428 Jülich, Germany

[b]Department of Physical Chemistry, University of Innsbruck, 6020 Innsbruck, Austria

[c]Institute of Physics, University of Graz, 8010 Graz, Austria

[d]Elettra-Sincrotrone Trieste S.C.p.A, Basovizza S.S. 14, Km 163.5, Trieste 34149, Italy

[e]Physics Department, University of Trieste, 34127 Trieste, Italy

[f]TASC Laboratory, CNR-IOM – Istituto Officina dei Materiali, 34149 Trieste, Italy

[g]Faculty of Physics and Center for Nanointegration Duisburg-Essen (CENIDE), University of Duisburg-Essen, 47048 Duisburg, Germany

[h]Department of Physics and Astronomy, UC Davis, Davis, CA 95616, USA

KEYWORDS: single-layer metal-organic framework, two-dimensional materials, scanning tunneling microscopy, angle-resolved photoelectron spectroscopy, absorption spectroscopy, band structure, charge transfer, density functional theory

ABSTRACT

Two-dimensional metal-organic frameworks (2D-MOFs) represent a category of atomically thin materials that combine the structural tunability of molecular systems with the crystalline structure characteristic of solids. The strong bonding between the organic linkers and transition metal centers is expected to result in delocalized electronic states. However, it remains largely unknown how band structure in 2D-MOFs emerges through the coupling of electronic states in the building blocks. Here, we demonstrate the on-surface synthesis of a 2D-MOF exhibiting prominent π-conjugation. Through a combined experimental and theoretical approach, we provide direct evidence of band structure formation upon hierarchical self-assembly, going from metal-organic complexes to a conjugated two-dimensional framework. Additionally, we identify the robustly dispersive nature of the new hybrid states, irrespective of the metallic support type, highlighting the tunability of the band structure through charge transfer from the substrate. Our findings encourage the exploration of band-structure engineering in 2D-MOFs for potential applications in electronics and photonics.

Supramolecular structures based on transition metals (TMs) coordinated with organic linkers offer a unique playground to create extended functional materials, with applications in catalysis, gas separation/ storage, sensing and energy harvesting/storage.[1–3] The structural tunability of those metal-organic frameworks (MOFs) originates from the choice of organic linkers with multiple coordination groups interconnecting transition metal centers to form stable and structures with high porosity and surface areas.[4] Due to their unique morphology MOFs have further emerged as templates in the synthesis of inorganic nanomaterials.[5–8] Steering the growth of MOFs on a solid surface offers the opportunity to steer the formation of two-dimensional MOFs (2D-MOFs).[9]Klicken oder tippen Sie hier, um Text einzugeben.
In this context, a thorough understanding of the interaction between the transition metal's 3d states with the π states of the ligand is critical, defining the electronic delocalization effects within the materials, and, thus, their functionality.[16,17] Specifically, π-conjugated MOFs offer exciting properties from high electric conductivity[18] and superconductivity,[19] to ferromagnetism.[20] Recently, not only the formation of dispersive band structure of on-surface stabilized MOFs have been reported,[15,17,21–26] but also ferromagnetic order[29] and Mott metal-insulator transitions.[28] Understanding how the band structure emerges in 2D-MOFs upon coupling of the building blocks is crucial for advancing materials design, enabling targeted manipulation of electronic properties for tailored applications in electronics and photonics.[27,28]

Here we investigated the emergence of electronic band structure upon hierarchical assembly of a 2D-MOFs supported on Au(111) and Ag(100) surfaces. The mixing of 3d states of Ni atoms with π-symmetric molecular orbitals (MOs) of 1,2,4,5-tetracyanobenzene (TCNB) allows obtaining π-delocalization. Local characterization of the metal-organic frameworks has been obtained by low-temperature scanning tunneling microscopy/spectroscopy (LT-STM/STS), in combination with

space-averaging methods, namely valence band (VB) angle-resolved photoelectron spectroscopy (ARPES), core level x-ray photoelectron spectroscopy (XPS) and near edge x-ray absorption fine structure (NEXAFS), which elucidate the electronic structure. The experimental results have been further corroborated with density functional theory (DFT) calculations and simulations within the framework of photoemission orbital tomography (POT), shedding light on the formation of dispersive electronic hybrid states in the 2D-MOF.

RESULTS AND DISCUSSION

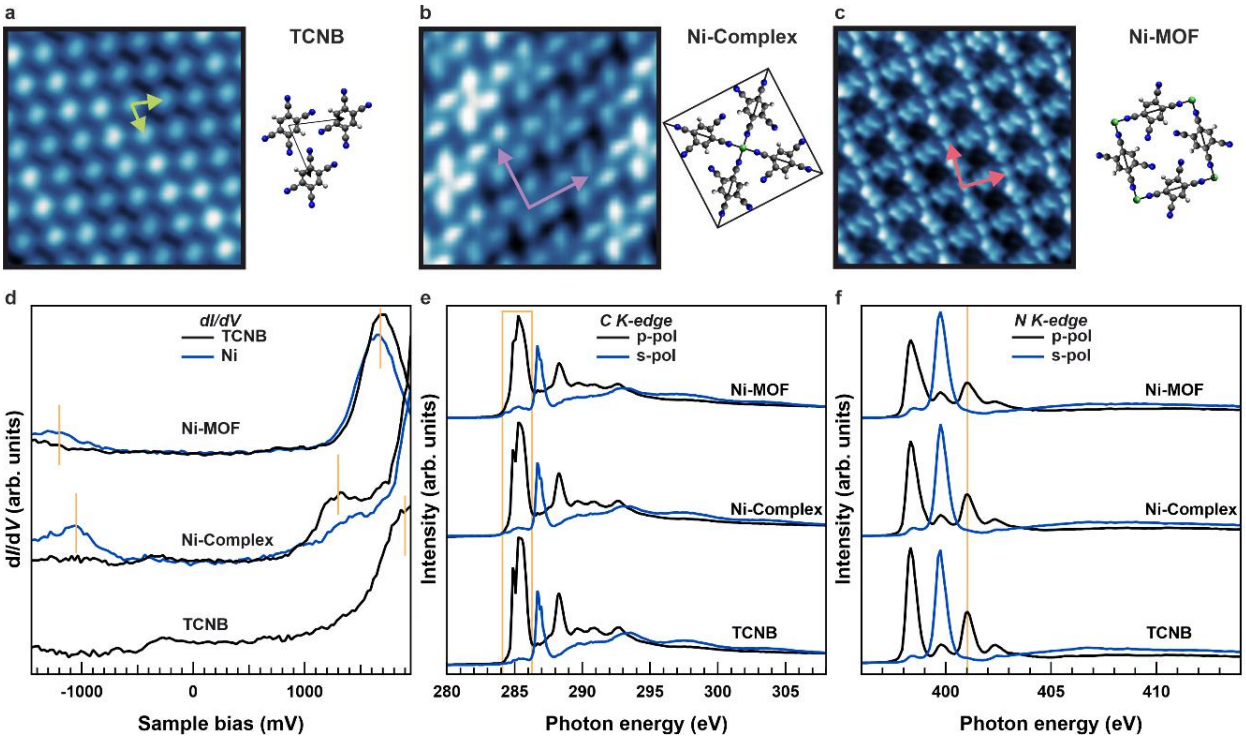

Figure 1. Topographic constant-current STM images (6.0 x 6.0 nm^2) acquired for the phases of interest: **a,** TCNB (V = 350 mV, I = 50 pA); **b,** Ni-Complex (V = 300 mV, I = 30 pA); **c,** Ni-MOF (V = 5 mV, I = 20 pA, molecule-functionalized tip). The unit cells and the corresponding structural models are also included. The unit cell of as-deposited TCNB on Au(111) can be described by two equivalent lattice vectors $a_{1,2}$ = 0.82 nm with a spanning angle α=74°. Both Ni-Complex and Ni-

MOF are square structures with $a = 1.70$ nm and $a = 1.16$ nm, respectively. **d,** dI/dV spectra acquired for TCNB, Ni-Complex and Ni-MOF. The feedback has been opened at $V = 400$ mV and $I = 50$ pA for all spectra. A voltage modulation of 30 mV at 759 Hz has been used. For the metal-organic structures, spectra have been collected both on Ni (blue) and TCNB (black). **e, f,** NEXAFS spectra acquired across the C and N K-edge for all phases of interest.

The formation of metal-organic nanostructures with controlled stoichiometry is initiated by the deposition of a monolayer of TCNB on Au(111) (see STM image in Fig. 1a), followed by the addition of Ni atoms. Maintaining the sample at 300 K for one hour results in thermodynamically stable metal-organic phases (Fig. 1b,c). Depending on the Ni amount, two different $Ni(TCNB)_x$ (x = 2, 4) phases can be resolved in STM images: while at low Ni coverages the $Ni(TCNB)_4$ phase is observed (Fig. 1b, "Ni-Complex"), the $Ni(TCNB)_2$ phase gradually starts to dominate with an increased Ni amount (Fig. 1c, "Ni-MOF"). This has been previously observed for metal-organic $Fe/Mn(TCNB)_x$ phases, with a structural adaption depending on the Fe(Mn)/TCNB ratio.[31,32] The Au(111) reconstruction is evident for all overlayers (Supporting Information S1), indicating a weak molecule-substrate interaction.[33,34] In both metal-organic phases (Fig. 1b, c), the Ni sites are in a square planar coordination environment, indicating a directional character of the interaction between the TCNB cyano (CN) groups and Ni centers.

After clarifying the geometric structure, the local electronic structure of the different phases has been elucidated by scanning tunneling spectroscopy (STS). Fig. 1d displays differential conductance spectra dI/dV acquired above the TCNB units (black) and Ni centers (blue). The spectrum of a TCNB monolayer on Au(111) is characterized by one main feature located at a voltage $V \approx 1900$ mV, being attributed to the lowest unoccupied molecular orbital (LUMO) of TCNB.[31] For the Ni-Complex, electronic states are detected at $V \approx -1050$ mV and $V \approx 1300$ mV,

while for the Ni-MOF, they lie at $V \approx$ -1200 mV and $V \approx$ 1680 mV. Such changes of the electronic states upon Ni coordination indicate the hybridization of Ni and TCNB states.[35,36] For the Ni-MOF, both occupied and unoccupied states are detected at the Ni sites (Fig. 1d), while the TCNB units exclusively accommodate the LUMO-derived state, as corroborated by constant-current dI/dV maps (Supporting Information S2).

To complement the STM/STS characterization, we have conducted NEXAFS experiments (Supporting Information S3), probing the on-surface orientation of the different functional TCNB constituents.[37] Fig. 1e, f display the NEXAFS spectra recorded across the C and N K-edge for TCNB, Ni-Complex and Ni-MOF on Au(111). In the C K-edge spectra, the region at ≈ 285 eV (Fig. 1e, orange box) is attributed to π*-symmetric resonances localized on the benzene ring.[38,39] The respective resonances are largely suppressed in s-polarization (blue) and only observed when using p-polarized light (black), suggesting that the benzene ring adsorbs flat on the surface without significant deformation.[40,41] Similarly, in the N K-edge spectra the π*-symmetric resonance at a photon energy ≈ 401 eV, associated with the CN groups of TCNB, is only observed in p-polarization (Fig. 1f, orange mark).[42] A flat on-surface orientation of the TCNB CN groups can accordingly be concluded. In all (metal-)organic phases, the orientations of the benzene ring and CN groups remain unaffected. Besides this geometric insight, the NEXAFS spectra reveal details on the electronic structure of the adsorbed TCNB units. Specifically, with an increasing Ni amount, the relative intensities of the π*-resonances compared to σ*-resonances are reduced. Note that the TCNB density per unit area does not differ between the different (metal-)organic layers (Supporting Information S1). Accordingly, the constant intensity of the σ*-resonances throughout all three interfaces clearly indicates that the Ni-induced structural adaptions do not result in an increased charge transfer from the substrate to the molecule. Instead, the quenching of π*-

resonances suggests a dominant π-symmetric Ni to TCNB bonding.[43] The intensity reduction involves resonances characteristic of both the benzene and CN constituents, implying a mixing of Ni states with the entire TCNB molecule. More details on how we distinguish the different phases during our measurements (NEXAFS/XPS, VB spectroscopy) are elaborated in the Supporting Information S3.

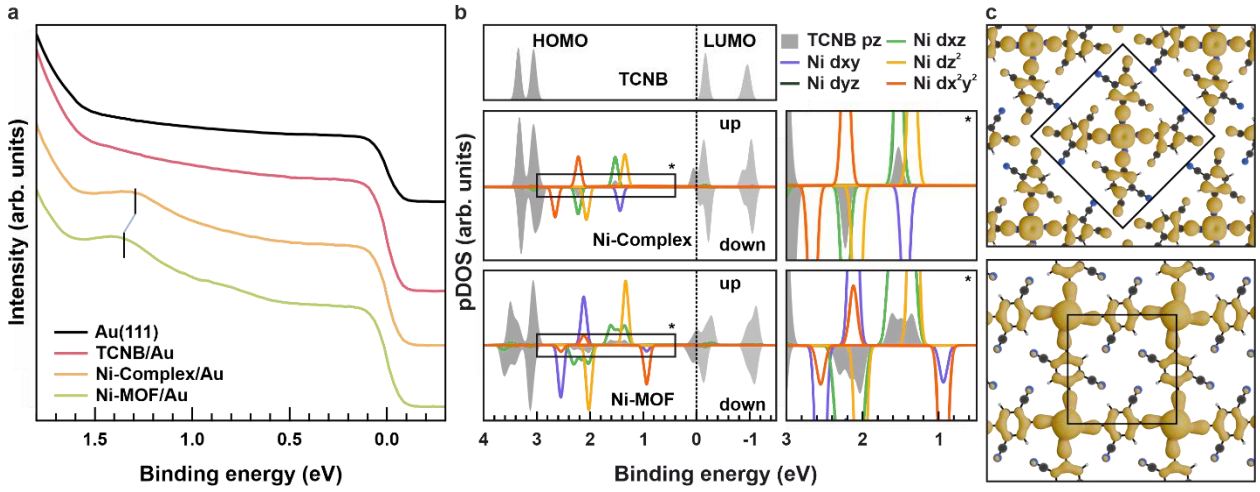

Figure 2. a, Angle-integrated VB photoemission spectra of Au(111) reference and all (metal-)organic phases of interest. All data have been obtained at a photon energy of 30 eV (p-polarization). **b,** Calculated gas-phase DOS projected onto Ni 3d and TCNB $2p_z$ states for TCNB, Ni-Complex and Ni-MOF (from top to bottom). Zoomed-in regions, marked by the starred rectangle, are shown to the right. **c,** Partial charge density (spin up) in the BE = 1.45-1.55 eV window for Ni-Complex (top) and in the BE = 1.27-1.37 eV window for Ni-MOF (bottom).

Intrigued by these findings, we have examined the Ni-TCNB interaction by analyzing the angle-integrated photoemission intensity in the VB region from the Fermi level (E_F) to a binding energy (BE) of 1.80 eV. Fig. 2a displays the VB spectra of Au(111) (top black line) and the (metal-)organic phases under investigation (colored lines). Depositing TCNB on Au(111) leads to no

apparent molecule-related features in this BE range, in agreement with the STS data (Fig. 1a). Note that at a BE of ≈ 1.50 eV the d-bands of the substrate start to dominate the spectrum and, therefore, do not allow a characterization of TCNB MOs beyond that BE. Supported by our DFT calculations below, we expect the photoemission signature related to the TCNB highest occupied MO (HOMO) in this energy region. Upon forming the Ni-Complex, a clear peak at a BE of ≈ 1.30 eV appears, which is shifted 50 meV towards higher BEs for the Ni-MOF. These observations support the emergence of a new metal-organic hybrid state upon creating the Ni-organic complex and framework. Furthermore, the change in BE evidences a qualitative difference between the isolated Ni-Complex and the extended Ni-MOF.

At this point, we turn to DFT calculations for a comprehensive interpretation. Using the structural information from STM and NEXAFS, we construct models of all phases and employ DFT to compute their energy level alignment. Given the weak interaction with the surface, and to put a focus on the new Ni-TCNB hybrid states, in a first step, all layers are treated as freestanding. The calculated spin-resolved density of states projected (pDOS) onto the Ni 3d (colored lines) and the TCNB $2p_z$ states (shaded grey) for the three systems are shown in Fig. 2b. Comparing the Ni-Complex and Ni-MOF to the pristine TCNB phase, states with strong Ni 3d-character are located at a BE ≈ 1.50 eV between the HOMO and LUMO of TCNB. Indeed, besides the expected Ni 3d-states, the calculations reveal a considerable contribution of TCNB $2p_z$ states at the same energies, suggesting a hybridization between the metal center and the TCNB ligands. Upon closer inspection (zoom in Fig. 2b), we find that the TCNB $2p_z$ states primarily hybridize with the Ni $3d_{xz/yz}$-levels (green lines). Moreover, our theoretical data predicts a notable energy broadening when going from the molecular Ni-Complex to the extended Ni-MOF (see also band structure plots in Supporting Information S4). This is further illustrated by the partial charge density of both Ni-

Complex and Ni-MOF presented in Fig 2c. Such a broadening is also predicted for TCNB LUMO/HOMO-based states with Ni $3d_{xz/yz}$-contributions.

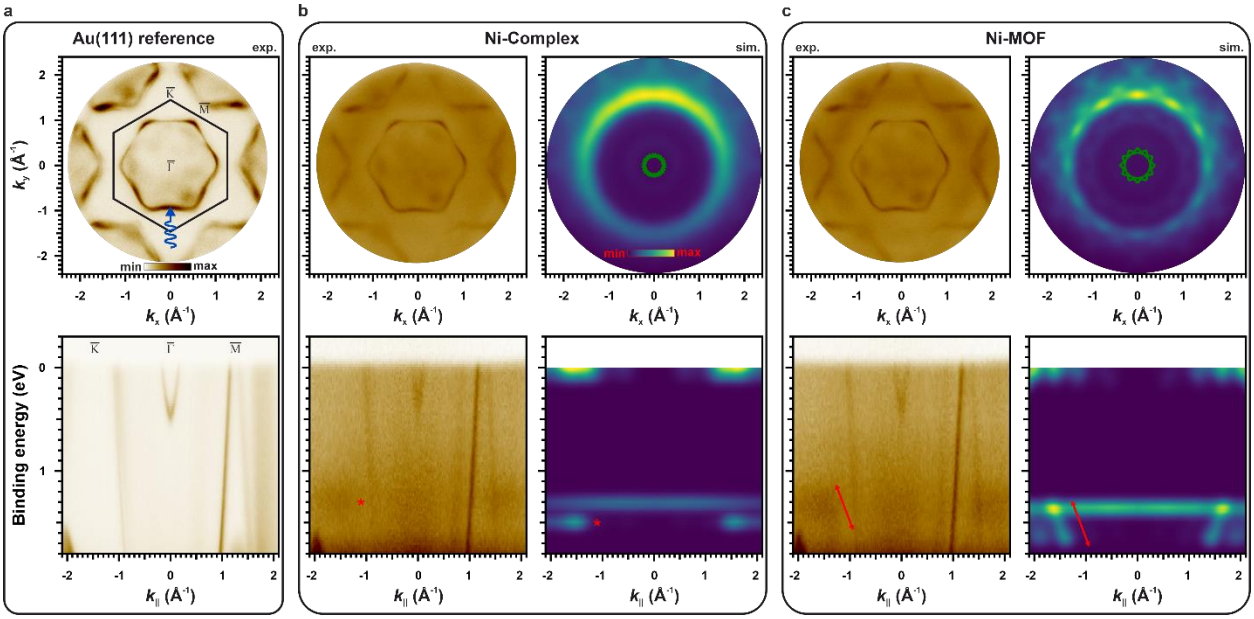

Figure 3. Top: Experimental constant BE momentum maps obtained for: **a,** Au(111); **b,** Ni-Complex/Au(111); **c,** Ni-MOF/Au(111). BE ≈ **a, b:** 1.30 eV; **c:** 1.35 eV. Simulated constant BE momentum maps for freestanding Ni-Complex and Ni-MOF are included in **b,** and **c,** for a BE = **c:** 1.45 eV; **d:** 1.50 eV. Bottom: Band maps along $\overline{K}$-$\overline{\Gamma}$-$\overline{M}$ of the substrate measured for: **a,** Au(111); **b,** Ni-Complex/Au(111); **c,** Ni-MOF/Au(111). Simulated band maps for freestanding Ni-Complex and Ni-MOF are included in **b,** and **c**. All experimental data have been collected at a photon energy of 30 eV (p-polarization).

To unambiguously identify the nature of the Ni 3d-based hybrid states, we employ POT, which links the angular distribution in constant BE photoemission intensity maps, so-called $k_{||}$ momentum maps, with the Fourier transform of the states they originate from.[44,45] Comparing measured and simulated $k_{||}$-maps, then allows for interpreting VB data in terms of molecular states. Using our

synchrotron-installed photoemission electron microscope (*k*-PEEM), we have measured complete momentum maps for $k_{||} < 2.20$ Å^{-1} across the presented BE range, leading to a three-dimensional (3D) intensity (k_x, k_y; BE) data set. The photoelectron $k_{||}$-distributions corresponding to the peak maxima in Fig. 2a are displayed for bare Au(111), Ni-Complex and Ni-MOF in Fig. 3 (top row, exp.). The precise orientation of the metal-organic structures with respect to the light incidence direction is possible from the features of Au(111) (indicated in Fig. 3a), still evident with adsorbed overlayers. The orientation found via STM (see Fig. 1 a-c) can be implemented accordingly,[46,47] further accounting for symmetry-equivalent orientations, whose Brillouin zones are highlighted in the simulated (sim.) emission patterns in the top panel of Fig. 3b, c. Upon forming the $Ni(TCNB)_x$ phases, an additional ring-like feature at ≈ 1.5 Å^{-1} appears. By comparing with the simulated momentum map, we find excellent agreement at a BE = 1.45 eV for Ni-Complex, where the hybridization of Ni $3d_{xz/yz}$ and ligand $2p_z$ states is strong, providing unambiguous evidence for the coordinative interaction between Ni and TCNB. Considering the experimental shift in BEs between Ni-Complex and Ni-MOF, we display the simulated map of Ni-MOF at a BE = 1.50 eV. The similar orientation of the coordinated Ni sites found via STM explains the similar shape of the momentum maps of Ni-Complex and Ni-MOF, likewise indicated by our theoretical data. For the Ni-MOF, the features are expected to become sharper in *k*-space because of the emerging extended π-conjugation. However, an appreciation of this effect solely on the momentum maps is difficult. The evident substrate features can be used to obtain $k_{||}$-distributions precisely along the same directions in *k*-space. In the bottom panel of Fig. 3 band maps, obtained through vertically cutting through our 3D data cube along $\overline{K}$-$\overline{\Gamma}$-$\overline{M}$ of the substrate, are displayed for clean Au(111) as well as $Ni(TCNB)_x$/Au(111) and compared to the calculated band maps. Apart from the energy shift between experiment and theory, the electronic level of the isolated Ni-Complex can be clearly

spotted (star) while the interconnected Ni-MOF exhibits signatures of band structure with clear signatures of sizeable dispersion (arrow), which can be appreciated, both, in the experimental and simulated band maps.

These findings are also remarkable from a different perspective. In previous works applying VB spectroscopy,[48–50] it has not been possible to detect emission features, which are that strongly related to d-orbitals of the metal center. The BE of the 3d-based states usually strongly overlaps with the highly intense substrate d-bands as, for instance, found for metalloporphyrins, which are POT prototype compounds.[51] Furthermore, photoemission from 3d-based states either occurs at $k_{||}$ values outside the experimentally accessible range or is easily mistaken as weak background for most transition metal complexes. Thus, no emissions are to be expected from the Ni $3d_{x2-y2/xy}$-based states, expected at a BE ≈ 0.95 eV according to the calculated pDOS in Fig. 2b. As evident from Supporting Information S4, these states mix with the TCNB $2p_{x,y}$-states to form states of σ-character, leading to emissions beyond our photoemission horizon of ≈ 2.20 $Å^{-1}$.[52] Notably, these localized states are not broadened in their energy width upon forming the extended Ni-MOF structure. The Ni $3d_{z^2}$-based DOS at a BE ≈ 1.35 eV in Fig. 2b appear as flat lines in Fig. 3c, but are not observed experimentally due to the missing contribution of TCNB 2p states to these levels. Notably, the unit cell of the Ni-MOF is mainly organic-based so that the intensity of its Ni 3d-based hybrid states emission features increases with significant ligand 2p contribution. In summary, the π-symmetric hybridization of Ni $3d_{xz/yz}$ states and TCNB p_z-based states is the important prerequisite that enables the observation of the electronic features here.

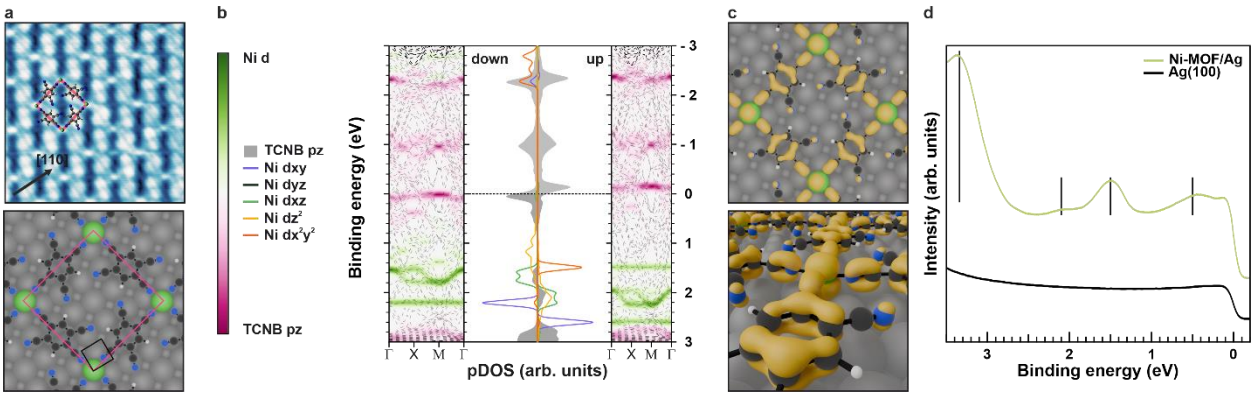

Figure 4. **a,** Top: High-resolution constant-current STM image (5.9 x 5.9 nm^2, V =40 mV and I =50 pA) of Ni-MOF on Ag(100), acquired with a CO-functionalized tip. Bottom: Relaxed structure of the Ni-MOF/Ag(100) interface. **b,** Calculated DOS and band structure projected on Ni 3d and TCNB 2p$_z$ states for Ni-MOF/Ag(100). **c,** Top and side views of the partial charge density (spin-up) in the BE = 1.95-2.05 eV window for Ni-MOF/Ag(100). **d,** Angle-integrated VB photoemission spectra of Ag(100) and Ni-MOF/Ag(100). All data have been obtained at a photon energy of 30 eV (p-polarization).

As our simulations for the freestanding layers correctly predict the observed Ni(I) oxidation state (Supporting Information S3) and lead to an excellent agreement with the experimental emission features for the Ni(TCNB)$_x$ structures on Au(111), we next explore the impact of more strongly interacting surfaces. According to literature, the structural motifs of various transition metal TCNB combinations are insensitive to the underlying support.[31,53–56] More reactive surfaces such as Ag substrates would allow us to focus on tuning the electronic properties of 2D-MOFs via charge

transfer.[51] Upon deposition of Ni onto TCNB/Ag(100), we find that the pristine TCNB layer is immediately converted into the extended Ni-MOF structure. Most importantly, the Ni-MOF forms a commensurate (4, -1; 1, 4) overlayer (see Supporting Information S5) on Ag(100), on whose characterization we focus in the following. Fig. 4a (top) shows a structural model overlayered to an STM image. To elucidate the impact of the Ag surface on the electronic structure of the Ni-MOF, the full interface including the substrate has been modelled (Fig. 4a, bottom). Compared to freestanding Ni-MOF, we find only negligible differences in the molecular arrangement. Given the similar structures, an energy-dispersive behavior of the electronic levels for Ni-MOF/Ag(100) is expected, as suggested by the calculated DOS and band structure of the interface projected onto the TCNB $2p_z$ and Ni 3d-states (Fig. 4b). In comparison to the pDOS of the freestanding Ni-MOF (Fig. 2b), the energy level alignment of the Ni 3d-states is indeed only slightly affected by the Ag substrate. The Ni(I) oxidation state predicted by our calculations is confirmed experimentally (Supporting Information S5). The stronger interaction with Ag, however, leads to overall larger band dispersions of the Ni-MOF states, as can be seen from the band structure plot in Fig. 4b (dashed lines), where the Ni-MOF character is highlighted by the color ranging from green (Ni 3d) to violet (TCNB $2p_z$). To highlight the similarity with the freestanding Ni-MOF, we illustrate the partial charge density in the BE = 1.95-2.05 eV window in Fig. 4c. We clearly observe the same hybridization between Ni $3d_{xz/yz}$ and TCNB $2p_z$ states. Interestingly, our simulations suggest the experimental appearance of the TCNB LUMO-based band due to charge transfer from the Ag surface, proving that the metal-organic nanostructures can be tuned via charge transfer at the interface while simultaneously retaining their π-conjugating properties. To test the theoretical predictions, we have measured the VB spectra of Ag(100) and Ni-MOF/Ag(100) (Fig. 4d). Compared to the uncovered Ag surface (black line), four prominent features arise and are indicated

by vertical bars at BEs of ≈ 0.50 eV, 1.50 eV, 2.10 eV and 3.30 eV. These experimental BEs are in good agreement with the states of the Ni-MOF, shown in the pDOS presented in Fig. 4c. Thus, we assign the features in the VB spectrum to a TCNB LUMO-based band contributing to intensity maxima at the E_F and a BE ≈ 0.50 eV, Ni 3d-based states (1.50 eV, 2.10 eV) and a TCNB HOMO-based band (3.30 eV). The fact that more Ni-MOF related emissions can be identified on Ag compared to Au is simply a result of the deeper lying onset of the Ag d-band (≈ 3.00 eV versus 1.50 eV for Au).

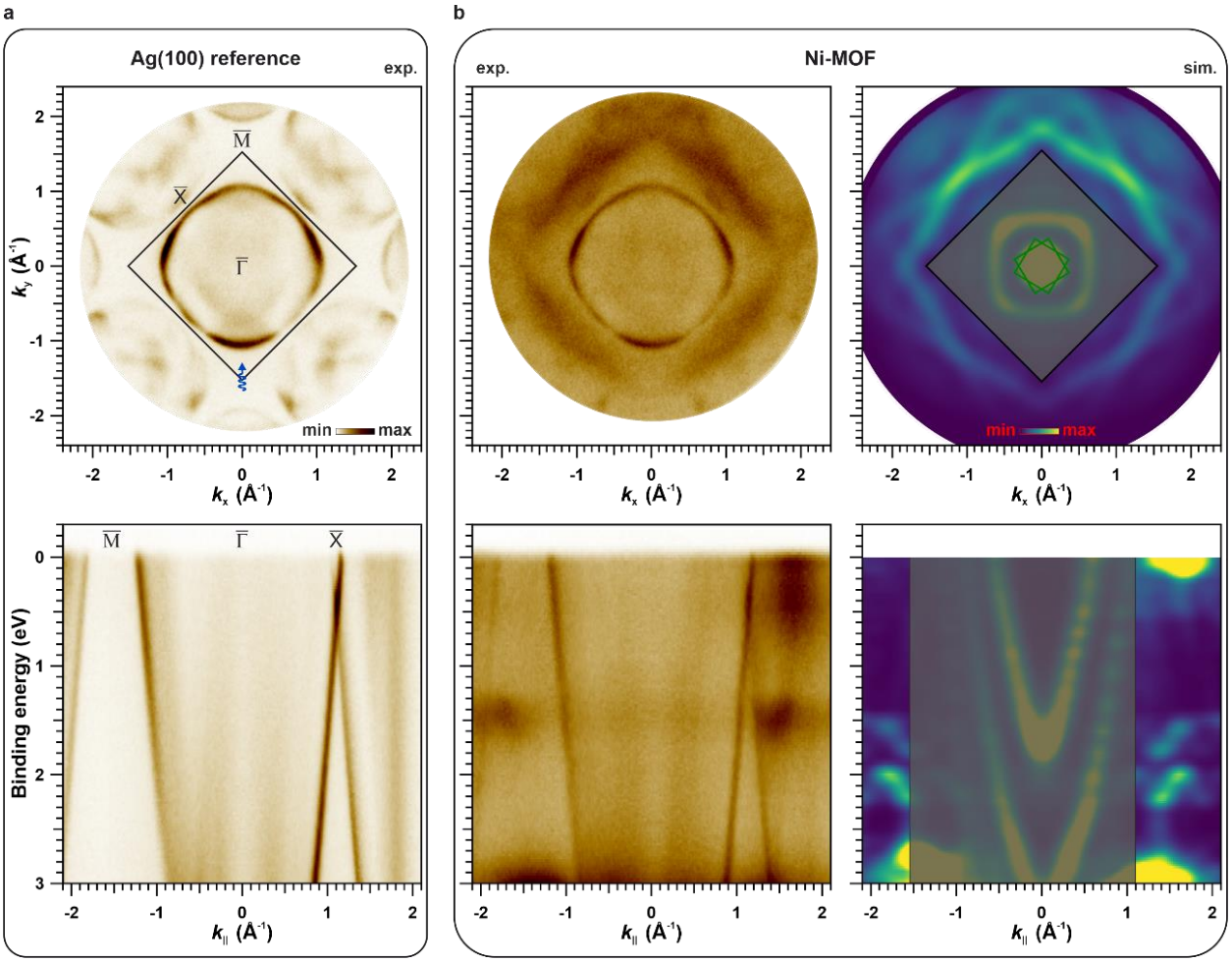

Figure 5. Top: Experimental constant BE ≈ 1.4 eV momentum maps for: **a,** Ag(100); **b,** Ni-MOF/Ag(100). A simulated constant BE = 1.55 eV momentum map for Ni-MOF/Ag is included

in **b**. Bottom: Band maps along $\overline{M}$-$\overline{\Gamma}$-$\overline{X}$ of the substrate for: **a,** Ag(100); **b,** Ni-MOF/Ag(100). A simulated band map for Ni-MOF/Ag(100) is included in **b**. All experimental data have been collected at a photon energy of 30 eV (p-polarization).

CONCLUSION

In conclusion, we have addressed how the coordinate bond between a TM center and its organic linker is characterized electronically and to what extent it is influenced by structural adaptions within metal-organic nanostructures. For low Ni amounts, a periodic layer with electronically isolated metal-organic $Ni(TCNB)_4$ complexes forms on Au(111). By increasing the Ni coverage, the formation of an extended $Ni(TCNB)_2$ MOF is observed. Notably, for the $Ni(TCNB)_2$ MOF, the π-delocalization throughout the structure leads to formation of dispersive electronic features. Finally, we demonstrate that the electronic structure of the 2D-MOF can be tuned via charge transfer from a more reactive Ag(100) substrate, where the $Ni(TCNB)_2$ framework is formed in controlled fashion. The findings presented here serve as a case study and can be applied to various coordination polymers, thereby paving the way towards a better band structure engineering in 2D-MOFs. Specifically for the $Ni(TCNB)_2$ 2D-MOF, an improvement in photocatalytic activity could be steered by the emergence of dispersive electronic states, as well by the interaction between substrate and MOF.[57] Furthermore, the influence of forming an extended and tunable MOF on the superexchange interactions between magnetic Ni cores for miniaturized magnetic devices may be further examined.[58,59] Finally, further studies targeting cyano-containing ligand-based MOFs [61] could lead to the discovery of π-conjugated 2D-MOFs with improved thermal stability.[60]

METHODS

Sample preparation

The Au(111) and Ag(100) single crystals have been cleaned by repeated cycles of Ar^+/Ne^+ sputtering (2.0/1.5 keV, $2\cdot10^{-6}/5\cdot10^{-7}$ mbar) followed by subsequent annealing to 773 K. Reference spectra and STM images have been collected in all setups used to confirm clean surfaces as starting point for further preparation. TCNB has been evaporated from a Knudsen-type evaporator at 373 K for 20 min onto the respective surfaces stabilized at 300 K. We found that TCNB does not form a second layer neither on Ag(100) nor on Au(111). Saturated TCNB layers have consequently been ensured by collecting photoelectron spectra whose shape does not change further when reaching a certain amount of signal characteristic of TCNB and topographic STM images of the pristine TCNB overlayers. Ni has been evaporated from similar evaporators based on electron beam heating with the flux monitored in the range of 5-10 nA and optimized for the preparation setup used. The structural rearrangement of TCNB is driven by the Ni amount, which allows for control over the metal-organic phase formed. The deposited Ni amounts are given in absolute times for clarity about the linear relationships and the sample has been stabilized at 300 K for every Ni deposition step. It has to be emphasized that within the multi-technique approach presented in this study different experimental setups have been used for which the necessary deposition times for Ni varied. In every experimental setup the Ni evaporation rates have been held constant so that the amounts are given in terms of absolute deposition times for every characterization step for a straightforward depiction of the relative Ni amounts.

LT-STM characterization

STM/STS experiments have been conducted using a commercial low-temperature STM (Infinity SPM, Scienta Omicron GmbH) in ultra-high vacuum ($p \approx 5 \cdot 10^{-10}$ mbar) and at a temperature $T \approx 8.5$ K. Bias voltage (V) is given as sample bias with respect to the tip. A small amount of CO has been dosed onto the cold surface ($T < 10$K) for tip functionalization. dI/dV spectroscopy has

been performed using lock-in detection of the tunneling current I by adding a sinusoidal voltage modulation at 759 Hz to the sample bias voltage V. Based on the variations from different line profiles used for structure determination, as well as comparison with literature on the TCNB/Au(111) interface,[31] we estimate an error of 7% and 5° for the lattice vectors and angles obtained, respectively. Ni-Complex and Ni-MOF have been the predominant phases present for total Ni deposition times of 30 s and 50 s, respectively.

VB spectroscopy

The data presented have been collected at the NanoESCA beamline of the synchrotron light source Elettra in Trieste, Italy. A *k*-PEEM (Focus GmbH NanoESCA II) that allows collecting the entire photoelectron hemisphere above the sample surface with angular resolution is installed there.[62] Varying the kinetic energy of the photoelectrons allows obtaining a 3D data stack constituted by 2D constant BE momentum maps. The angle-integrated VB spectra display the BE dependence of the integrated intensity of each of these discs. ARPES band maps represent vertical cuts through this 3D dataset at defined $k_{\parallel}$ paths. A photon energy of 30 eV (p-polarization) has been used for characterization. The photon angle of incidence with respect to the surface normal has been 65°. Measurements have been conducted at a $p < 1 \cdot 10^{-10}$ mbar after the sample has been cooled down to 90 K. The energy-resolution and *k*-resolution have been 100 meV and ± 0.05 $Å^{-1}$, respectively. The motorized sample positioning system installed within the setup allows to continuously raster the sample during characterization damage induced by the beam is impeded and high-quality data can be obtained. The angle-integrated VB spectra of clean Au(111) and Ag(100) have been divided by a factor of four in order to allow a better comprehensibility of the data.

NEXAFS and XPS

Absorption and core level photoelectron spectroscopy measurements have been performed at the ALOISA beamline of the synchrotron light source Elettra in Trieste, Italy.[63] Samples have been characterized at 300 K and $p < 1 \cdot 10^{-10}$ mbar. BEs have been calibrated using the photoelectron lines of the supporting substrates.[64,65] The normalization and energy calibration protocol for the absorption spectra collected is described elsewhere.[66] Photoelectron spectra haven been collected using p-polarized light. A normal emission geometry has been realized, with the photon propagation axis on the sample at a grazing incidence (86° with respect to surface normal). At a photon energy of 515 (980) eV, used for XPS, the overall energy resolution has been 160 (420) meV. NEXAFS spectra have been collected by partial electron yield mode with a channeltron, equipped with a repelling grid polarized at a negative bias (-250 V and -370 V for the C and N K-edge, ~~respectively~~ -820 V for the Ni L_3-edge). The sample has been kept at an 84° grazing photon incidence with respect to the surface normal and the manipulator has been mounted along the photon propagation axis. The surface orientation with respect to the linearly polarized light has been changed via rotation around the photon axis from Transverse Electric (s-polarization) to Transverse Magnetic (closely p-polarization).

LEED characterization

A commercial LEED setup (SPECS GmbH) has been used to characterize the sample crystallinity. When examining the relative changes characteristic of the transformations within (metal-)organic layers, the sample-to-electron source distance and the incident beam energy have been kept constant. This ensures that changes in LEED patterns are only attributed to structural changes.

Theoretical modelling

We have conducted ground state density functional theory (DFT) calculations using the Vienna Ab-initio Simulation Package (VASP) versions 6.4.1 on the Vienna Scientific Cluster 5 (VSC-5)

and 5.4.4 on VSC-4.[67,68] The exchange-correlation effects have been incorporated via the Perdew-Burke-Enzerdorf generalized gradient approximation (PBE-GGA)[69] with a Grimme D3 van der Waals correction with Becke-Johnson damping.[70] Within such an GGA-type xc-function, the inclusion of some form of self-interaction error correction for the strongly localized d-orbitals in the transition metal is crucial for an accurate model of the hybridization observed in the experiments. Therefore, we added an effective Hubbard-U parameter of 3 eV using the Dudarev ansatz.[71] Starting with the experimentally determined structures, we fully relaxed all systems until all atomic forces are below 0.01 eV/Å. We modeled the interface in the repeated slab approach with a 15 Å vacuum layer, adding a dipole layer within the vacuum region to address the electric field discrepancy between either side of the slab.[72] The bulk of the silver substrate has been represented by five layers in total, allowing relaxation only in the top two layers during geometry optimization. The first Brillouin zone has been sampled using a Γ-centered 8x8x1 grid. For the simulation of the photoelectron distribution, the photoemission process has been simulated as a one-step process where we approximated the final state as a plane wave. Additionally, we included a damping of the substrate emissions according to Ref.[73] of $\Gamma = 0.5$ Å^{-1}.

ASSOCIATED CONTENT

Supporting Information. Details on the orientation of the (metal-)organic phases with respect to their Au(111) support; *dI/dV* mapping characterization of Ni-MOF/Au(111); Additional spectroscopic characterization underlining the applicability of space-averaging methods; Additional calculation results; Templating properties of the TCNB/Ag(100) interface.

AUTHOR INFORMATION

Corresponding Authors

*d.baranowski@fz-juelich.de; v.feyer@fz-juelich.de; peter.puschnig@uni-graz.at; laerte.patera@uibk.ac.at

Present Address

†Photon Science Division, Paul Scherrer Institute, 5232 Villigen PSI, Switzerland

Author Contributions

Da.B., M.T. and L.L.P. performed STM/STS experiments and analysis, with essential contributions of V.C. to the analysis. Da.B., I. C., V. F., L.S., L.F., and C.G.B conducted NEXAFS experiments, analyzed by Da.B. with feedback from all people involved in NEXAFS experiments. Da.B., I.C., S.M., and V.F. performed VB spectroscopy experiments, analyzed by Da.B. with feedback from all people involved in NEXAFS experiments. Do.B., A.W., P.P performed the DFT calculations and simulations in the POT framework. Da.B. wrote the first draft of the manuscript with essential contributions of M.T., L.L.P., Do.B., A.W., V.F. and P.P.. V.F. and C.M.S. supervised the project. The manuscript was improved through contributions of all authors. All authors have given approval to the final version of the manuscript.

Notes

The authors declare no competing financial interests.

ACKNOWLEDGMENTS

Da.B., I.C., S.M. and V.F. acknowledge Elettra Synchrotron Trieste for providing access to its synchrotron radiation facilities. Part of the shown data has been obtained at the ALOISA beamline through funding from the European Union's Horizon 2020 research and innovation program under

grant agreement No 101007417, having benefitted from the access provided by CNR-IOM in Trieste within the framework of the NFFA-Europe Pilot Transnational Access Activity, proposal ID400. Do.B, A.W. and P.P. acknowledge support from the European Research Council (ERC) Synergy Grant, Project ID 101071259, and the Vienna Scientific Cluster (VSC) for providing the computational resources. M.T. and L.L.P. acknowledge support from the ERC under the European Union's Horizon 2020 research and innovation programme (grant agreement no. 101039746) funded by the European Union.

ABBREVIATIONS

2D, two-dimensional; MOF, metal-organic framework, TM, transition metal; MO, molecular orbital; LT, low-temperature; STM/STS, scanning tunneling microscopy/spectroscopy; VB, valence band; ARPES, angle-resolved photoelectron spectroscopy, XPS, x-ray photoelectron spectroscopy; NEXAFS, near edge x-ray absorption fine structure; DFT, density functional theory; POT, photoemission orbital tomography; BE, binding energy; LEED, low-energy electron diffraction.

REFERENCES

(1) Furukawa, H.; Cordova, K. E.; O'Keeffe, M.; Yaghi, O. M. The Chemistry and Applications of Metal-Organic Frameworks. *Science (1979)* **2013**, *341* (6149), 1230444. https://doi.org/10.1126/science.1230444.

(2) Li, D.; Yadav, A.; Zhou, H.; Roy, K.; Thanasekaran, P.; Lee, C. Advances and Applications of Metal-Organic Frameworks (MOFs) in Emerging Technologies: A Comprehensive Review. *Global Challenges* **2024**, *8* (2). https://doi.org/10.1002/gch2.202300244.

(3) Hajivand, P.; Carolus Jansen, J.; Pardo, E.; Armentano, D.; Mastropietro, T. F.; Azadmehr, A. Application of Metal-Organic Frameworks for Sensing of VOCs and Other Volatile Biomarkers. *Coord Chem Rev* **2024**, *501*, 215558. https://doi.org/10.1016/j.ccr.2023.215558.

(4) Zhou, H.-C.; Long, J. R.; Yaghi, O. M. Introduction to Metal–Organic Frameworks. *Chem Rev* **2012**, *112* (2), 673–674. https://doi.org/10.1021/cr300014x.

(5) Shen, K.; Chen, X.; Chen, J.; Li, Y. Development of MOF-Derived Carbon-Based Nanomaterials for Efficient Catalysis. *ACS Catal* **2016**, *6* (9), 5887–5903. https://doi.org/10.1021/acscatal.6b01222.

(6) Kaneti, Y. V.; Dutta, S.; Hossain, Md. S. A.; Shiddiky, M. J. A.; Tung, K.; Shieh, F.; Tsung, C.; Wu, K. C. -W.; Yamauchi, Y. Strategies for Improving the Functionality of Zeolitic Imidazolate Frameworks: Tailoring Nanoarchitectures for Functional Applications. *Advanced Materials* **2017**, *29* (38). https://doi.org/10.1002/adma.201700213.

(7) Indra, A.; Song, T.; Paik, U. Metal Organic Framework Derived Materials: Progress and Prospects for the Energy Conversion and Storage. *Advanced Materials* **2018**, *30* (39). https://doi.org/10.1002/adma.201705146.

(8) Salunkhe, R. R.; Kaneti, Y. V.; Yamauchi, Y. Metal–Organic Framework-Derived Nanoporous Metal Oxides toward Supercapacitor Applications: Progress and Prospects. *ACS Nano* **2017**, *11* (6), 5293–5308. https://doi.org/10.1021/acsnano.7b02796.

(9) Barth, J. V.; Costantini, G.; Kern, K. Engineering Atomic and Molecular Nanostructures at Surfaces. *Nature* **2005**, *437* (7059), 671–679. https://doi.org/10.1038/nature04166.

(10) Wang, Z. F.; Liu, Z.; Liu, F. Organic Topological Insulators in Organometallic Lattices. *Nat Commun* **2013**, *4* (1), 1471. https://doi.org/10.1038/ncomms2451.

(11) Wang, Z. F.; Su, N.; Liu, F. Prediction of a Two-Dimensional Organic Topological Insulator. *Nano Lett* **2013**, *13* (6), 2842–2845. https://doi.org/10.1021/nl401147u.

(12) Dong, L.; Kim, Y.; Er, D.; Rappe, A. M.; Shenoy, V. B. Two-Dimensional π-Conjugated Covalent-Organic Frameworks as Quantum Anomalous Hall Topological Insulators. *Phys Rev Lett* **2016**, *116* (9), 096601. https://doi.org/10.1103/PhysRevLett.116.096601.

(13) Zhang, L. Z.; Wang, Z. F.; Huang, B.; Cui, B.; Wang, Z.; Du, S. X.; Gao, H.-J.; Liu, F. Intrinsic Two-Dimensional Organic Topological Insulators in Metal–Dicyanoanthracene Lattices. *Nano Lett* **2016**, *16* (3), 2072–2075. https://doi.org/10.1021/acs.nanolett.6b00110.

(14) Sun, H.; Tan, S.; Feng, M.; Zhao, J.; Petek, H. Deconstruction of the Electronic Properties of a Topological Insulator with a Two-Dimensional Noble Metal–Organic Honeycomb–Kagome Band Structure. *The Journal of Physical Chemistry C* **2018**, *122* (32), 18659–18668. https://doi.org/10.1021/acs.jpcc.8b03353.

(15) Liu, J.; Lin, N. On-Surface-Assembled Single-Layer Metal-Organic Frameworks with Extended Conjugation. *Chempluschem* **2023**, *88* (5). https://doi.org/10.1002/cplu.202200359.

(16) Santhini, V. M.; Wäckerlin, C.; Cahlík, A.; Ondráček, M.; Pascal, S.; Matěj, A.; Stetsovych, O.; Mutombo, P.; Lazar, P.; Siri, O.; Jelínek, P. 1D Coordination π–d Conjugated Polymers with Distinct Structures Defined by the Choice of the Transition Metal: Towards a New Class of Antiaromatic Macrocycles. *Angewandte Chemie International Edition* **2021**, *60* (1), 439–445. https://doi.org/10.1002/anie.202011462.

(17) Liu, J.; Abel, M.; Lin, N. On-Surface Synthesis: A New Route Realizing Single-Layer Conjugated Metal–Organic Structures. *J Phys Chem Lett* **2022**, *13* (5), 1356–1365. https://doi.org/10.1021/acs.jpclett.1c04134.

(18) Huang, X.; Sheng, P.; Tu, Z.; Zhang, F.; Wang, J.; Geng, H.; Zou, Y.; Di, C.; Yi, Y.; Sun, Y.; Xu, W.; Zhu, D. A Two-Dimensional π–d Conjugated Coordination Polymer with Extremely High Electrical Conductivity and Ambipolar Transport Behaviour. *Nat Commun* **2015**, *6* (1), 7408. https://doi.org/10.1038/ncomms8408.

(19) Huang, X.; Zhang, S.; Liu, L.; Yu, L.; Chen, G.; Xu, W.; Zhu, D. Superconductivity in a Copper(II)-Based Coordination Polymer with Perfect Kagome Structure. *Angewandte Chemie International Edition* **2018**, *57* (1), 146–150. https://doi.org/10.1002/anie.201707568.

(20) Dong, R.; Zhang, Z.; Tranca, D. C.; Zhou, S.; Wang, M.; Adler, P.; Liao, Z.; Liu, F.; Sun, Y.; Shi, W.; Zhang, Z.; Zschech, E.; Mannsfeld, S. C. B.; Felser, C.; Feng, X. A Coronene-Based Semiconducting Two-Dimensional Metal-Organic Framework with Ferromagnetic Behavior. *Nat Commun* **2018**, *9* (1), 2637. https://doi.org/10.1038/s41467-018-05141-4.

(21) Jakub, Z.; Shahsavar, A.; Planer, J.; Hrůza, D.; Herich, O.; Procházka, P.; Čechal, J. How the Support Defines Properties of 2D Metal–Organic Frameworks: Fe-TCNQ on Graphene versus Au(111). *J Am Chem Soc* **2024**, *146* (5), 3471–3482. https://doi.org/10.1021/jacs.3c13212.

(22) Kraus, S.; Herman, A.; Huttmann, F.; Bianchi, M.; Stan, R.-M.; Holt, A. J.; Tsukamoto, S.; Rothenbach, N.; Ollefs, K.; Dreiser, J.; Bischof, K.; Wende, H.; Hofmann, P.; Atodiresei, N.; Michely, T. Uniaxially Aligned 1D Sandwich-Molecular Wires: Electronic Structure and Magnetism. *The Journal of Physical Chemistry C* **2022**, *126* (6), 3140–3150. https://doi.org/10.1021/acs.jpcc.1c10625.

(23) Hernández-López, L.; Piquero-Zulaica, I.; Downing, C. A.; Piantek, M.; Fujii, J.; Serrate, D.; Ortega, J. E.; Bartolomé, F.; Lobo-Checa, J. Searching for Kagome Multi-Bands and Edge States in a Predicted Organic Topological Insulator. *Nanoscale* **2021**, *13* (10), 5216–5223. https://doi.org/10.1039/D0NR08558H.

(24) Frezza, F.; Schiller, F.; Cahlík, A.; Ortega, J. E.; Barth, J. V.; Arnau, A.; Blanco-Rey, M.; Jelínek, P.; Corso, M.; Piquero-Zulaica, I. Electronic Band Structure of 1D π–d Hybridized Narrow-Gap Metal–Organic Polymers. *Nanoscale* **2023**, *15* (5), 2285–2291. https://doi.org/10.1039/D2NR05828F.

(25) Kumar, A.; Banerjee, K.; Foster, A. S.; Liljeroth, P. Two-Dimensional Band Structure in Honeycomb Metal–Organic Frameworks. *Nano Lett* **2018**, *18* (9), 5596–5602. https://doi.org/10.1021/acs.nanolett.8b02062.

(26) Zhang, R.; Liu, J.; Gao, Y.; Hua, M.; Xia, B.; Knecht, P.; Papageorgiou, A. C.; Reichert, J.; Barth, J. V.; Xu, H.; Huang, L.; Lin, N. On-surface Synthesis of a Semiconducting 2D Metal–Organic Framework $Cu_3(C_6O_6)$ Exhibiting Dispersive Electronic Bands. *Angewandte Chemie International Edition* **2020**, *59* (7), 2669–2673. https://doi.org/10.1002/anie.201913698.

(27) Cahlík, A.; Ondráček, M.; Wäckerlin, C.; Solé, A. P.; Siri, O.; Švec, M.; Jelínek, P. Light-Controlled Multiconfigurational Conductance Switching in a Single 1D Metal–Organic Wire. *ACS Nano* **2024**, *18* (13), 9576–9583. https://doi.org/10.1021/acsnano.3c12909.

(28) Lowe, B.; Field, B.; Hellerstedt, J.; Ceddia, J.; Nourse, H. L.; Powell, B. J.; Medhekar, N. V.; Schiffrin, A. Local Gate Control of Mott Metal-Insulator Transition in a 2D Metal-Organic Framework. *Nat Commun* **2024**, *15* (1), 3559. https://doi.org/10.1038/s41467-024-47766-8.

(29) Lobo-Checa, J.; Hernández-López, L.; Otrokov, M. M.; Piquero-Zulaica, I.; Candia, A. E.; Gargiani, P.; Serrate, D.; Delgado, F.; Valvidares, M.; Cerdá, J.; Arnau, A.; Bartolomé, F. Ferromagnetism on an Atom-Thick & Extended 2D Metal-Organic Coordination Network. *Nat Commun* **2024**, *15* (1), 1858. https://doi.org/10.1038/s41467-024-46115-z.

(30) Luo, L.; Hou, L.; Cui, X.; Zhan, P.; He, P.; Dai, C.; Li, R.; Dong, J.; Zou, Y.; Liu, G.; Liu, Y.; Zheng, J. Self-Condensation-Assisted Chemical Vapour Deposition Growth of Atomically Two-Dimensional MOF Single-Crystals. *Nat Commun* **2024**, *15* (1), 3618. https://doi.org/10.1038/s41467-024-48050-5.

(31) Kezilebieke, S.; Amokrane, A.; Boero, M.; Clair, S.; Abel, M.; Bucher, J.-P. Steric and Electronic Selectivity in the Synthesis of Fe-1,2,4,5-Tetracyanobenzene (TCNB) Complexes on Au(111): From Topological Confinement to Bond Formation. *Nano Res* **2014**, *7* (6), 888–897. https://doi.org/10.1007/s12274-014-0450-y.

(32) Piantek, M.; Serrate, D.; Moro-Lagares, M.; Algarabel, P.; Pascual, J. I.; Ibarra, M. R. Manganese Phthalocyanine Derivatives Synthesized by On-Surface Cyclotetramerization. *The Journal of Physical Chemistry C* **2014**, *118* (31), 17895–17899. https://doi.org/10.1021/jp506652j.

(33) Faraggi, M. N.; Jiang, N.; Gonzalez-Lakunza, N.; Langner, A.; Stepanow, S.; Kern, K.; Arnau, A. Bonding and Charge Transfer in Metal–Organic Coordination Networks on Au(111) with Strong Acceptor Molecules. *The Journal of Physical Chemistry C* **2012**, *116* (46), 24558–24565. https://doi.org/10.1021/jp306780n.

(34) Torrente, I. F.; Franke, K. J.; Pascual, J. I. Structure and Electronic Configuration of Tetracyanoquinodimethane Layers on a Au(111) Surface. *Int J Mass Spectrom* **2008**, *277* (1–3), 269–273. https://doi.org/10.1016/j.ijms.2008.07.013.

(35) Albrecht, F.; Neu, M.; Quest, C.; Swart, I.; Repp, J. Formation and Characterization of a Molecule–Metal–Molecule Bridge in Real Space. *J Am Chem Soc* **2013**, *135* (24), 9200–9203. https://doi.org/10.1021/ja404084p.

(36) Repp, J.; Meyer, G.; Paavilainen, S.; Olsson, F. E.; Persson, M. Imaging Bond Formation Between a Gold Atom and Pentacene on an Insulating Surface. *Science (1979)* **2006**, *312* (5777), 1196–1199. https://doi.org/10.1126/science.1126073.

(37) Cudia, C. C.; Vilmercati, P.; Larciprete, R.; Cepek, C.; Zampieri, G.; Sangaletti, L.; Pagliara, S.; Verdini, A.; Cossaro, A.; Floreano, L.; Morgante, A.; Petaccia, L.; Lizzit, S.; Battocchio, C.; Polzonetti, G.; Goldoni, A. Electronic Structure and Molecular Orientation

of a Zn-Tetra-Phenyl Porphyrin Multilayer on Si(111). *Surf Sci* **2006**, *600* (18), 4013–4017. https://doi.org/10.1016/j.susc.2006.01.115.

(38) Bässler, M.; Fink, R.; Buchberger, C.; Väterlein, P.; Jung, M.; Umbach, E. Near Edge X-Ray Absorption Fine Structure Resonances of Quinoide Molecules. *Langmuir* **2000**, *16* (16), 6674–6681. https://doi.org/10.1021/la0002536.

(39) Fraxedas, J.; Lee, Y. J.; Jiménez, I.; Gago, R.; Nieminen, R. M.; Ordejón, P.; Canadell, E. Characterization of the Unoccupied and Partially Occupied States of TTF-TCNQ by XANES and First-Principles Calculations. *Phys Rev B* **2003**, *68* (19), 195115. https://doi.org/10.1103/PhysRevB.68.195115.

(40) Stöhr, J.; Outka, D. A. Determination of Molecular Orientations on Surfaces from the Angular Dependence of Near-Edge x-Ray-Absorption Fine-Structure Spectra. *Phys Rev B* **1987**, *36* (15), 7891–7905. https://doi.org/10.1103/PhysRevB.36.7891.

(41) Pettersson, L. G. M.; Ågren, H.; Luo, Y.; Triguero, L. Benzene Adsorbed on Cu(110): Theoretical X-Ray Absorption, Emission and Shake Calculations. *Surf Sci* **1998**, *408* (1–3), 1–20. https://doi.org/10.1016/S0039-6028(98)00085-5.

(42) Chernenkaya, A.; Medjanik, K.; Nagel, P.; Merz, M.; Schuppler, S.; Canadell, E.; Pouget, J.-P.; Schönhense, G. Nature of the Empty States and Signature of the Charge Density Wave Instability and Upper Peierls Transition of TTF-TCNQ by Temperature-Dependent NEXAFS Spectroscopy. *Eur Phys J B* **2015**, *88* (1), 13. https://doi.org/10.1140/epjb/e2014-50481-9.

(43) Ruehl, E.; Hitchcock, A. P. Carbon K-Shell Excitation of Metallocenes. *J Am Chem Soc* **1989**, *111* (14), 5069–5075. https://doi.org/10.1021/ja00196a008.

(44) Puschnig, P.; Berkebile, S.; Fleming, A. J.; Koller, G.; Emtsev, K.; Seyller, T.; Riley, J. D.; Ambrosch-Draxl, C.; Netzer, F. P.; Ramsey, M. G. Reconstruction of Molecular Orbital Densities from Photoemission Data. *Science (1979)* **2009**, *326* (5953), 702–706. https://doi.org/10.1126/science.1176105.

(45) Puschnig, P.; Ramsey, M. G. Photoemission Tomography: Valence Band Photoemission as a Quantitative Method for Investigating Molecular Films. In *Encyclopedia of Interfacial Chemistry*; Elsevier, 2018; pp 380–391. https://doi.org/10.1016/B978-0-12-409547-2.13782-5.

(46) Fujita, D.; Amemiya, K.; Yakabe, T.; Nejoh, H.; Sato, T.; Iwatsuki, M. Observation of Two-Dimensional Fermi Contour of a Reconstructed Au(111) Surface Using Fourier Transform Scanning Tunneling Microscopy. *Surf Sci* **1999**, *423* (2–3), 160–168. https://doi.org/10.1016/S0039-6028(98)00886-3.

(47) Reinert, F.; Nicolay, G. Influence of the Herringbone Reconstruction on the Surface Electronic Structure of Au(111). *Applied Physics A* **2004**, *78* (6), 817–821. https://doi.org/10.1007/s00339-003-2436-6.

(48) Zamborlini, G.; Lüftner, D.; Feng, Z.; Kollmann, B.; Puschnig, P.; Dri, C.; Panighel, M.; Di Santo, G.; Goldoni, A.; Comelli, G.; Jugovac, M.; Feyer, V.; Schneider, C. M. Multi-Orbital Charge Transfer at Highly Oriented Organic/Metal Interfaces. *Nat Commun* **2017**, *8* (1), 335. https://doi.org/10.1038/s41467-017-00402-0.

(49) Cojocariu, I.; Sturmeit, H. M.; Zamborlini, G.; Cossaro, A.; Verdini, A.; Floreano, L.; D'Incecco, E.; Stredansky, M.; Vesselli, E.; Jugovac, M.; Cinchetti, M.; Feyer, V.; Schneider, C. M. Evaluation of Molecular Orbital Symmetry via Oxygen-Induced Charge Transfer Quenching at a Metal-Organic Interface. *Appl Surf Sci* **2020**, *504* (504), 144343. https://doi.org/10.1016/j.apsusc.2019.144343.

(50) Sturmeit, H. M.; Cojocariu, I.; Jugovac, M.; Cossaro, A.; Verdini, A.; Floreano, L.; Sala, A.; Comelli, G.; Moro, S.; Stredansky, M.; Corva, M.; Vesselli, E.; Puschnig, P.; Schneider, C. M.; Feyer, V.; Zamborlini, G.; Cinchetti, M. Molecular Anchoring Stabilizes Low Valence Ni(<scp>i</Scp>)TPP on Copper against Thermally Induced Chemical Changes. *J Mater Chem C Mater* **2020**, *8* (26), 8876–8886. https://doi.org/10.1039/D0TC00946F.

(51) Sturmeit, H. M.; Cojocariu, I.; Windischbacher, A.; Puschnig, P.; Piamonteze, C.; Jugovac, M.; Sala, A.; Africh, C.; Comelli, G.; Cossaro, A.; Verdini, A.; Floreano, L.; Stredansky, M.; Vesselli, E.; Hohner, C.; Kettner, M.; Libuda, J.; Schneider, C. M.; Zamborlini, G.; Cinchetti, M.; Feyer, V. Room-Temperature On-Spin-Switching and Tuning in a Porphyrin-Based Multifunctional Interface. *Small* **2021**, *17* (50), 2104779. https://doi.org/10.1002/smll.202104779.

(52) Haags, A.; Yang, X.; Egger, L.; Brandstetter, D.; Kirschner, H.; Bocquet, F. C.; Koller, G.; Gottwald, A.; Richter, M.; Gottfried, J. M.; Ramsey, M. G.; Puschnig, P.; Soubatch, S.; Tautz, F. S. Momentum Space Imaging of σ Orbitals for Chemical Analysis. *Sci Adv* **2022**, *8* (29). https://doi.org/10.1126/sciadv.abn0819.

(53) Koudia, M.; Abel, M. Step-by-Step on-Surface Synthesis: From Manganese Phthalocyanines to Their Polymeric Form. *Chem. Commun.* **2014**, *50* (62), 8565–8567. https://doi.org/10.1039/C4CC02792B.

(54) Kezilebieke, S.; Amokrane, A.; Abel, M.; Bucher, J.-P. Hierarchy of Chemical Bonding in the Synthesis of Fe-Phthalocyanine on Metal Surfaces: A Local Spectroscopy Approach. *J Phys Chem Lett* **2014**, *5* (18), 3175–3182. https://doi.org/10.1021/jz5015696.

(55) Abel, M.; Clair, S.; Ourdjini, O.; Mossoyan, M.; Porte, L. Single Layer of Polymeric Fe-Phthalocyanine: An Organometallic Sheet on Metal and Thin Insulating Film. *J Am Chem Soc* **2011**, *133* (5), 1203–1205. https://doi.org/10.1021/ja108628r.

(56) Giovanelli, L.; Savoyant, A.; Abel, M.; Maccherozzi, F.; Ksari, Y.; Koudia, M.; Hayn, R.; Choueikani, F.; Otero, E.; Ohresser, P.; Themlin, J.-M.; Dhesi, S. S.; Clair, S. Magnetic Coupling and Single-Ion Anisotropy in Surface-Supported Mn-Based Metal–Organic Networks. *The Journal of Physical Chemistry C* **2014**, *118* (22), 11738–11744. https://doi.org/10.1021/jp502209q.

(57) Liu, H.; Cheng, M.; Liu, Y.; Wang, J.; Zhang, G.; Li, L.; Du, L.; Wang, G.; Yang, S.; Wang, X. Single Atoms Meet Metal–Organic Frameworks: Collaborative Efforts for Efficient

Photocatalysis. *Energy Environ Sci* **2022**, *15* (9), 3722–3749. https://doi.org/10.1039/D2EE01037B.

(58) Abdurakhmanova, N.; Tseng, T.-C.; Langner, A.; Kley, C. S.; Sessi, V.; Stepanow, S.; Kern, K. Superexchange-Mediated Ferromagnetic Coupling in Two-Dimensional Ni-TCNQ Networks on Metal Surfaces. *Phys Rev Lett* **2013**, *110* (2), 027202. https://doi.org/10.1103/PhysRevLett.110.027202.

(59) Faraggi, M. N.; Golovach, V. N.; Stepanow, S.; Tseng, T.-C.; Abdurakhmanova, N.; Kley, C. S.; Langner, A.; Sessi, V.; Kern, K.; Arnau, A. Modeling Ferro- and Antiferromagnetic Interactions in Metal–Organic Coordination Networks. *The Journal of Physical Chemistry C* **2015**, *119* (1), 547–555. https://doi.org/10.1021/jp512019w.

(60) Tseng, T.-C.; Abdurakhmanova, N.; Stepanow, S.; Kern, K. Hierarchical Assembly and Reticulation of Two-Dimensional Mn- and Ni–TCNQ $_x$ ($x = 1, 2, 4$) Coordination Structures on a Metal Surface. *The Journal of Physical Chemistry C* **2011**, *115* (20), 10211–10217. https://doi.org/10.1021/jp2033643.

(61) Wei, Y.; Ren, X.; Ma, H.; Sun, X.; Zhang, Y.; Kuang, X.; Yan, T.; Wu, D.; Wei, Q. In Situ Formed Co(TCNQ) $_2$ Metal-Organic Framework Array as a High-Efficiency Catalyst for Oxygen Evolution Reactions. *Chemistry – A European Journal* **2018**, *24* (9), 2075–2079. https://doi.org/10.1002/chem.201705606.

(62) Wiemann, C.; Patt, M.; Krug, I. P.; Weber, N. B.; Escher, M.; Merkel, M.; Schneider, C. M. A New Nanospectroscopy Tool with Synchrotron Radiation: NanoESCA@Elettra. *e-Journal of Surface Science and Nanotechnology* **2011**, *9*, 395–399. https://doi.org/10.1380/ejssnt.2011.395.

(63) Floreano, L.; Naletto, G.; Cvetko, D.; Gotter, R.; Malvezzi, M.; Marassi, L.; Morgante, A.; Santaniello, A.; Verdini, A.; Tommasini, F.; Tondello, G. Performance of the Grating-Crystal Monochromator of the ALOISA Beamline at the Elettra Synchrotron. *Review of Scientific Instruments* **1999**, *70* (10), 3855–3864. https://doi.org/10.1063/1.1150001.

(64) Anthony, M. T.; Seah, M. P. XPS: Energy Calibration of Electron Spectrometers. 1—An Absolute, Traceable Energy Calibration and the Provision of Atomic Reference Line Energies. *Surface and Interface Analysis* **1984**, *6* (3), 95–106. https://doi.org/10.1002/sia.740060302.

(65) Seah, M. P.; Gilmore, I. S.; Beamson, G. XPS: Binding Energy Calibration of Electron Spectrometers 5?Re-Evaluation of the Reference Energies. *Surface and Interface Analysis* **1998**, *26* (9), 642–649. https://doi.org/10.1002/(SICI)1096-9918(199808)26:9<642::AID-SIA408>3.0.CO;2-3.

(66) Floreano, L.; Cossaro, A.; Gotter, R.; Verdini, A.; Bavdek, G.; Evangelista, F.; Ruocco, A.; Morgante, A.; Cvetko, D. Periodic Arrays of Cu-Phthalocyanine Chains on Au(110). *The Journal of Physical Chemistry C* **2008**, *112* (29), 10794–10802. https://doi.org/10.1021/jp711140e.

(67) Kresse, G.; Hafner, J. *Ab Initio* Molecular Dynamics for Liquid Metals. *Phys Rev B* **1993**, *47* (1), 558–561. https://doi.org/10.1103/PhysRevB.47.558.

(68) Kresse, G.; Joubert, D. From Ultrasoft Pseudopotentials to the Projector Augmented-Wave Method. *Phys Rev B* **1999**, *59* (3), 1758–1775. https://doi.org/10.1103/PhysRevB.59.1758.

(69) Perdew, J. P.; Burke, K.; Ernzerhof, M. Generalized Gradient Approximation Made Simple. *Phys Rev Lett* **1996**, *77* (18), 3865–3868. https://doi.org/10.1103/PhysRevLett.77.3865.

(70) Grimme, S.; Ehrlich, S.; Goerigk, L. Effect of the Damping Function in Dispersion Corrected Density Functional Theory. *J Comput Chem* **2011**, *32* (7), 1456–1465. https://doi.org/10.1002/jcc.21759.

(71) Dudarev, S. L.; Botton, G. A.; Savrasov, S. Y.; Humphreys, C. J.; Sutton, A. P. Electron-Energy-Loss Spectra and the Structural Stability of Nickel Oxide: An LSDA+U Study. *Phys Rev B* **1998**, *57* (3), 1505–1509. https://doi.org/10.1103/PhysRevB.57.1505.

(72) Neugebauer, J.; Scheffler, M. Adsorbate-Substrate and Adsorbate-Adsorbate Interactions of Na and K Adlayers on Al(111). *Phys Rev B* **1992**, *46* (24), 16067–16080. https://doi.org/10.1103/PhysRevB.46.16067.

(73) Lüftner, D.; Weiß, S.; Yang, X.; Hurdax, P.; Feyer, V.; Gottwald, A.; Koller, G.; Soubatch, S.; Puschnig, P.; Ramsey, M. G.; Tautz, F. S. Understanding the Photoemission Distribution of Strongly Interacting Two-Dimensional Overlayers. *Phys Rev B* **2017**, *96* (12), 125402. https://doi.org/10.1103/PhysRevB.96.125402.

TABLE OF CONTENTS ENTRY